

Integral imaging based 3D display of holographic data

Ali Özgür Yöntem* and Levent Onural

Department of Electrical and Electronics Engineering, Bilkent University, TR-06800 Bilkent, Ankara, Turkey

*Corresponding author: aozgur@ee.bilkent.edu.tr

Abstract: We propose a method and present applications of this method that converts a diffraction pattern into an elemental image set in order to display them on an integral imaging based display setup. We generate elemental images based on diffraction calculations as an alternative to commonly used ray tracing methods. Ray tracing methods do not accommodate the interference and diffraction phenomena. Our proposed method enables us to obtain elemental images from a holographic recording of a 3D object/scene. The diffraction pattern can be either numerically generated data or digitally acquired optical data. The method shows the connection between a hologram (diffraction pattern) and an elemental image set of the same 3D object. We showed three examples, one of which is the digitally captured optical diffraction tomography data of an epithelium cell. We obtained optical reconstructions with our integral imaging display setup where we used a digital lenslet array. We also obtained numerical reconstructions, again by using the diffraction calculations, for comparison. The digital and optical reconstruction results are in good agreement.

© 2012 Optical Society of America

OCIS codes: (110.0110) Imaging systems; (110.4190) Multiple imaging; (110.6880) Three-dimensional image acquisition.

References and links

1. G. Lippmann, "La photographie intégrale," C.R. Hebd. Seances Acad. Sci. **146**, 446–451 (1908).
2. F. Okano, H. Hoshino H. A. Jun, and I. Yuyama, "Real-time pickup method for a three-dimensional image based on the integral photography," Appl. Opt. **36**, 1–14 (1997).
3. S. S. Athineos, N. P. Sgouros, P. G. Papageorgas, D. E. Maroulis, M. S. Sangriotis, and N. G. Theofanous, "Photorealistic integral photography using a ray-traced model of capturing optics," J. Electron Imaging **15**, 0430071–0430078 (2006).
4. S.-W. Min, K. S. Park, B. Lee, Y. Cho, and M. Hahn, "Enhanced image mapping algorithm for computer-generated integral imaging system," Jpn. J. Appl. Phys. **45**, L744–L747 (2006).
5. S.-H. Lee, S.-C. Kim, and E.-S. Kim, "Reconstruction of digital hologram generated by sub-image of integral imaging," Proc. of SPIE **6912**, 69121F1–69121F10 (2008).
6. S.-W. Min, S. Jung, J.-H. Park, and B. Lee, "Three-dimensional display system based on computer-generated integral photography," Proc. of SPIE **4297**, 187–195 (2001).
7. J.-K. Lee, S.-C. Kim, and E.-S. Kim, "Reconstruction of three-dimensional object and system analysis using ray tracing in practical integral imaging system," Proc. of SPIE **6695**, 6695191–66951912 (2007).
8. B.-N.-R. Lee, Y. Cho, K. S. Park, S.-W. Min, J.-S. Lim, M. C. Whang, and K. R. Park, "Design and implementation of a fast integral image rendering method," Lect. Notes Comput. Sc. **4161**, 135–140 (2006).
9. U. Schnars and W. P. O. Jüptner, "Digital recording and numerical reconstruction of holograms," Meas. Sci. and Tech. **13**, R85–R110 (2002).
10. L. Onural, "Sampling of the diffraction field," Appl. Opt. **39**, 5929–5935 (2000).
11. A. Ö. Yöntem and Levent Onural, "Integral imaging using phase-only LCoS spatial light modulators as Fresnel lenslet arrays," J. Opt. Soc. Am. A **28**, 2359–2375 (2011).

12. B. E. A. Saleh and M. C. Teich, *Fundamentals of Photonics* (John Wiley and Sons, Inc., 1991).
13. J. W. Goodman, *Introduction to Fourier Optics* (Mc-Graw-Hill, 1996).
14. T. Mishina, M. Okui, and F. Okano, "Generation of holograms using integral photography," *Proc. of SPIE* **5599**, 114–122 (2004).
15. R. V. Pole, "3-D imagery and holograms of objects illuminated in white light," *Appl. Phys. Lett.* **10**, 20–22 (1967).
16. B. Javidi and S.-H. Hong, "Three-dimensional holographic image sensing and integral imaging display," *J. Disp. Technol* **1**, 341–346 (2005).
17. C. Quan, X. Kang, and C. J. Tay, "Speckle noise reduction in digital holography by multiple holograms," *Opt. Eng.* **46** 1158011–1158016 (2007).
18. J. G.-Sucerquia, J. A. H. Ramírez, and D. V. Prieto, "Reduction of speckle noise in digital holography by using digital image processing," *Optik* **116**, 44–48 (2005).
19. T. Baumbach, E. Kolenović, V. Kebbel, and W. Jüptner, "Improvement of accuracy in digital holography by use of multiple holograms," *Appl. Opt.* **45**, 6077–6085 (2006).
20. T. Ito and K. Okano, "Color electroholography by three colored reference lights simultaneously incident upon one hologram panel," *Opt. Express* **12**, 4320–4325 (2004).
21. F. Yaraş and L. Onural, "Color holographic reconstruction using multiple SLMs and LED illumination," *Proc. of SPIE* **7237**, 7237001–7237005 (2010).
22. I. Bergoënd, C. Arfire, N. Pavillon, and C. Depeursinge, "Diffraction tomography for biological cells imaging using digital holographic microscopy," *Proc. of SPIE* **7376**, 7376131–7376138 (2010).
23. D. Mas, J. Garcia, C. Ferreira, L. M. Bernardo, and F. Marinho, "Fast algorithms for free-space diffraction patterns calculation," *Opt. Commun.* **164**, 233–245 (1999).
24. H. Kang, T. Fujii, T. Yamaguchi, and H. Yoshikawa, "Compensated phase-added stereogram for real-time holographic display," *Opt. Eng.* **46**, 0958021–09580211 (2007).
25. T. Shimobaba, T. Ito, N. Masuda, Y. Abe, Y. Ichihashi, H. Nakayama, N. Takada, A. Shiraki, and T. Sugie, "Numerical calculation library for diffraction integrals using the graphic processing unit: the GPU-based wave optics library," *J. Opt. A-Pure and Appl. Opt.* **10**, 0753081–0753085 (2009).
26. J.-S. Jang and B. Javidi, "Three-dimensional integral imaging with electronically synthesized lenslet arrays," *Opt. Lett.* **27**, 1767–1769 (2002).
27. M. Kovachev, R. Ilieva, P. Benzie, G. B. Esmer, L. Onural, J. Watson, and T. Reyhan, "Holographic 3DTV displays using spatial light modulators," in *Three-Dimensional Television-Capture, Transmission, Display*, H. Ozaktas, and L. Onural, eds. (Springer, 2008), pp. 529–555.
28. L. Onural, F. Yaraş, and H. Kang, "Digital holographic three-dimensional video displays," *Proc. of IEEE* **99**, 576–589 (2011).
29. F. Yaraş, H. Kang, and L. Onural, "Circular holographic video display system," *Opt. Express* **19**, 9147–9156 (2011).
30. S.-W. Min, S. Jung, H. Choi, Y. Kim, J.-H. Park, and B. Lee, "Wide-viewing-angle integral three-dimensional imaging system by curving a screen and a lens array," *Appl. Opt.* **44**, 546–552 (2005).
31. D.-H. Shin, B.-G. Lee, J. Hyun, D.-C. Hwang, and E.-S. Kim, "Curved projection integral imaging using an additional large-aperture convex lens for viewing angle improvement," *ETRI J.* **31**, 105–110 (2009).

1. Introduction

Integral imaging is a promising 3D capture and display system. Conventional integral imaging systems are composed of two stages: a pick-up system to obtain elemental images of a 3D object/scene and a display stage which integrates the elemental images for reconstruction [1]. These parts are physical optical setups. These setups are usually not end-to-end, that is, two setups are separate. In the capture part, the elemental images are imaged by means of a series of lenses and a lenslet array, on a CCD array or a digital camera. In the display setup, the obtained elemental images are displayed on a LCD and the reconstruction is observed through a lenslet array. It is necessary to match the size of the captured elemental images on the CCD to the displayed ones on the LCD in the display setup since the physical sizes of the devices are usually different. Furthermore, the pixel size of the CCD sensor does matter since the quality of the reconstruction depends on it. Finally, the LCD panel in the display setup should be able to accommodate all of the captured elemental images. To display a good quality still 3D image or a video sequence, both setups require usual adjustments and alignments (imaging distances, magnification ratios, etc.) of optical elements. Such a work is studied rigorously in [2]. That work is an example for the case where optically captured elemental images of a physical 3D

object are reconstructed optically at the display end. Such integral imaging systems consist of decoupled capture and display units, and therefore, both units need careful adjustments. For applications such as 3D gaming, 3D modeling, animation, etc., the only physically needed part is the display. In those systems, the elemental images are digitally obtained for synthetic 3D objects and then displayed on an optical display setup. Digital techniques are more flexible compared to optical capture processes. If the elemental images are obtained by computation, optical adjustments are needed only for the display part. Ray tracing methods can be used to generate elemental images. There are many reported studies using ray tracing methods to obtain elemental images for computer generated integral imaging systems [3–7]. The capture process, for computer generated integral imaging systems, is performed using certain computer graphics algorithms such as point retracing rendering, multiple viewpoint rendering, parallel group rendering, viewpoint vector rendering, etc., [8]. All of these algorithms are based on ray tracing.

In our work, as an alternative method to generate elemental images, we performed diffraction calculations using wave propagation methods based on the Fresnel kernel. To the best of our knowledge, such an approach is not reported before. One can compute the scalar field distribution in the space using the Fresnel propagation model [9, 10]. We can generate elemental images by first modeling the optical system with image processing tools and then by applying optical wave propagation principles [11]. Wave propagation models accommodate diffraction and interference phenomena whereas ray models do not [12, 13]. Wave propagation models are especially useful for the cases where we have holographic data of a 3D object/scene. This is in fact an inverse problem of hologram generation from elemental images [5, 14, 15]; that is, we obtain elemental images from a holographic recording as in [16].

There are certain problems with direct optical reconstruction from holographic data by holographic means, such as speckle noise due to coherent illumination. Thus, certain image processing techniques (filtering and averaging) are usually performed to remove the noise and to reconstruct the data digitally [17–19]. This way, the visibility in digital reconstructions can be improved. However, in holographic optical reconstructions, speckle noise is present due to coherent illumination. In our case, at least on the display side, we do not have additional speckle noise problem since we use incoherent illumination for the reconstructions.

It is not desirable to use lasers for the reconstruction due to potential hazards to the eye, either. It may be possible to use LED illumination to avoid laser hazards while observing the holographic reconstructions [20, 21]. However, the reconstruction quality would be lower due to spectral properties of the light source.

On the other hand, integral imaging works primarily with incoherent illumination. It may be desirable to reconstruct holographic data by an integral imaging display. A conversion from holographic data to elemental image data is needed to reconstruct the 3D image using incoherent light and integral imaging techniques. Such an idea is studied in [16]. In that work, first a series of images are reconstructed at different depths, creating a set of slices of 3D data. Then, the elemental images are generated using another process which maps each slice to the elemental image plane. Instead of such an approach, we directly use holographic data to display 3D images on an integral imaging setup. For this purpose, we designed a direct pick-up integral imaging capture system, [6]. This digital pick-up system is realized solely by a computer program that simulates wave propagation. Lenslet arrays that we used in the design are composed of digital synthetic Fresnel thin lenslets [11]. We processed the input holographic data with this simulator to obtain computer generated elemental images. This way, we generate the elemental images in one step. We used these computer generated elemental images in a physical display setup to reconstruct optically 3D images. In our proposed display, we used a modified version of the setup given in [11] where we replaced the analog lenslet array with a digitally controlled

synthetic Fresnel lenslet array written on a phase-only LCoS SLM. By this procedure, we can generate elemental images digitally from recorded holographic input data and optically reconstruct a 3D image from them on our integral imaging display. For example, our method can be used to generate elemental images from holograms captured within a diffraction tomography setup [22].

In some cases, diffraction calculation might be slower than ray tracing calculations. There are several fast algorithms which implement diffraction calculations based on the Fresnel kernel [23]. Even real-time diffraction calculations are possible [24]. Indeed, one of the implementations uses the graphical processing unit to further increase the computation speed [25]. Our elemental image generation method is quite similar to techniques used in digital hologram generation procedures. We calculated the diffraction fields using DFT. We computed the DFT using an FFT algorithm. It is possible to apply other abovementioned faster algorithms to our case, as well. However, the comparison of the effects of such different computational procedures to the performance is not a part of this study.

Presented numerical and optical results show that the computationally generated elemental images using wave propagation principle from synthetic or real objects can be used to successfully reconstruct 3D images. Furthermore, a digitally controlled synthetic lenslet array can be used at the display stage setup of an integral imaging system [11, 26].

In Section 2 we describe the proposed system. We explain the method to obtain elemental images and present the optical setup that we use to reconstruct the 3D objects. In Section 3, we show the optical display experiment results of the proposed system together with the computer simulations. Finally, we draw conclusions, with notes, in the last section.

2. Proposed system

In this section, we present the method for elemental image generation from holographic data and an integral imaging optical setup to reconstruct 3D images from the computer generated elemental images. The holographic data may be acquired either by optical means or computed using digital techniques. We present our method in the first subsection. In the second subsection, we present the algorithm and in the third subsection we present three examples. In the first example, we obtain the elemental images of two letters at different depths. We first generated the diffraction patterns (computer generated holograms) of the letters. The complex diffraction pattern is then used as the input to our algorithm. The output of the algorithm gives the elemental image set of these letters at the imaging distance. For the second example, we obtain the elemental images of a 3D pyramid shaped object. In the last example, we obtain the set of elemental images as the output from a digitally captured optical holographic data which is obtained using a diffraction tomography technique [22]; the object is an epithelium cell. In the last subsection, we describe the optical setup which we used to reconstruct the 3D image from elemental images. Thus we show that the obtained elemental images can be used for optical reconstruction. The object sizes and display distances should match the optical setup requirements. Thus, the holographic data should be further processed if the object sizes and the distances do not match the display system. This processing is especially needed for optically captured holographic data.

2.1. The method

Suppose we have digitally recorded holographic data (diffraction data) of a 3D object; a setup is shown in Fig. 1(a). Since, our aim is to display 3D image of a holographically recorded object/scene data by using an integral imaging technique, we need to convert the holographic data to elemental images. An in-line hologram of a 3D object is related to the diffraction field of that object [10]. This diffraction field can either be obtained digitally by calculating the propagation

of light field scattered from the object or captured by optical means. In Fig. 1(a), a sketch of the diffraction pattern at $z = z_0$ of a cube is shown. In Fig. 1(b), a generic setup is demonstrated to holographically reconstruct the 3D image of the original object. In a digital holographic display system, diffraction field is sampled and written on a SLM. When the SLM is illuminated by a laser light source, an observer can perceive the 3D image [27]. For the integral imaging setup,

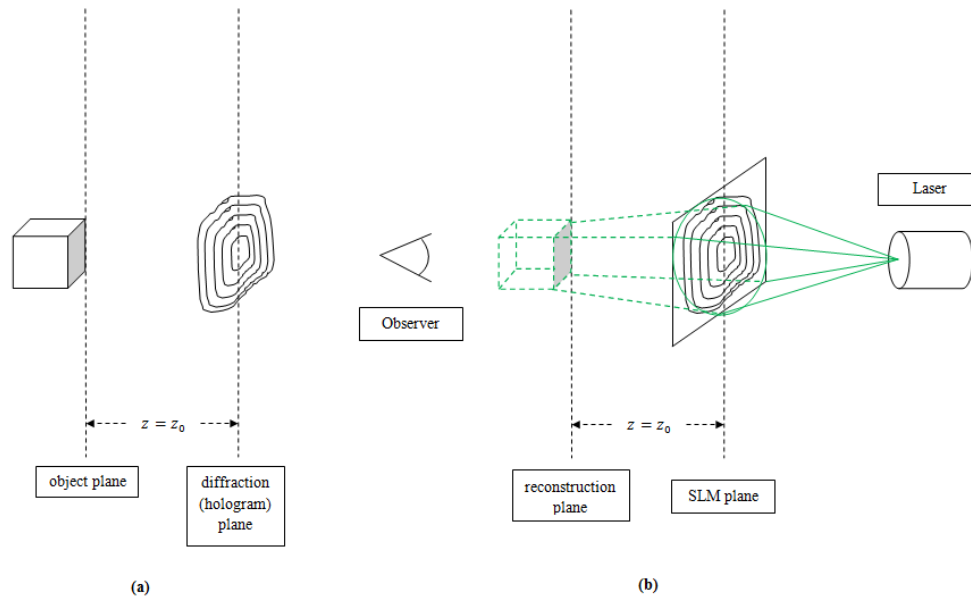


Fig. 1. (a) A generic sketch of holographic recording. The diffraction pattern at $z = z_0$ is captured. (b) A generic sketch of 3D image reconstruction from the captured hologram.

to find the elemental images of a 3D object numerically, we used the block diagram depicted in Fig. 2(c) that is designed based on the capture setup of a generic integral imaging system shown in Fig. 2(a). We assume that the light field scattered from the object is available as diffraction data at the input. We obtained the elemental images by first calculating the Fresnel propagation of this data to the lenslet array plane, $z = d$, and then by multiplying this field by the lenslet array phase pattern, and finally, by computationally propagating the resulting field once more by a distance $z = g$, where $1/g = 1/f - 1/d$, f is the focal length of a single lenslet [11]. In Fig. 2(b), reconstruction of the 3D image at the display part of a generic integral imaging system is shown. The observer perceives a pseudoscopic 3D reconstruction due to the nature of direct pick-up method used in the capture part of the integral imaging system. It is easy to process the elemental images to set orthoscopic 3D images instead of pseudoscopic version [2]. To relate the diffraction data of a 3D object and the elemental images of the same 3D object, let us examine the setups in Fig. 1(a) and Fig. 2(a). Suppose that the wavelength is the same during recording and reconstruction. In the integral imaging system, the diffraction pattern just before the lenslet array is needed to find the elemental images as described above. If we have the 2D diffraction field at a certain distance, we can find the 2D diffraction field of the same object at another distance by calculating the free space propagation. So, the field just before the lenslet array is related to the diffraction pattern at the distance $z = z_0$ and can be found by propagating this diffraction field by another distance $z = d - z_0$. However, we might have an input diffraction pattern obtained from a holographic setup with a different wavelength than the one used in the integral imaging display system. In that case we need to pre-process the input data.

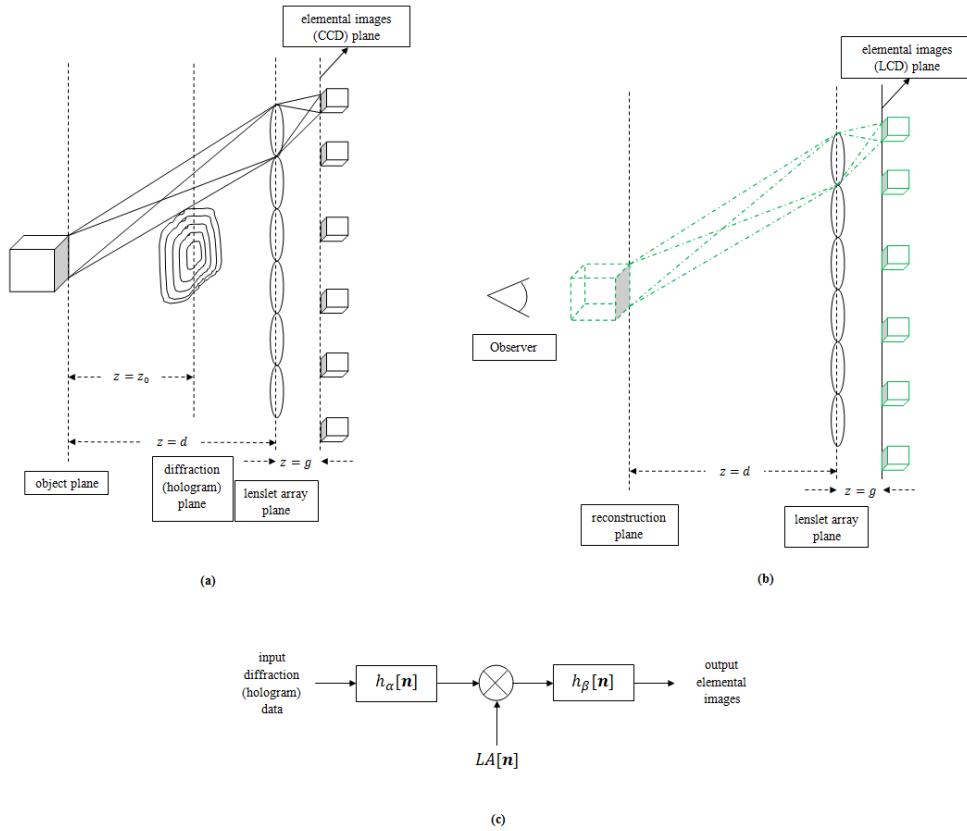


Fig. 2. (a) A generic integral imaging data capture setup. The diffraction pattern in Fig.1 (a) is also depicted. For the same object with the same physical dimensions, the diffraction patterns in both systems are the same. (b) A generic Integral imaging display setup. The reconstruction is pseudoscopic due to employed direct pick-up method.(c) Designed model to calculate elemental images from diffraction (hologram) data.

The impulse response of the continuous Fresnel kernel is

$$h(\mathbf{x}) = \frac{1}{j\lambda z} \exp\left(j\frac{2\pi}{\lambda}z\right) \exp\left(j\frac{\pi}{\lambda z}\mathbf{x}^T\mathbf{x}\right) \quad (1)$$

where $\mathbf{x} = [x \ y]^T$, x and y are the transversal spatial domain variables, z is the distance parameter and λ is the wavelength [10]. The scalar wave propagation can be modeled as a linear shift invariant system with the impulse response given by Eq. (1). Naturally, discretizations are needed for computer simulations. For this reason we model the analog system given in Fig. 2(a) as a discrete system given in Fig. 2(c). Here the two blocks represent discrete linear shift invariant systems with impulse responses $h_\alpha[\mathbf{n}]$ and $h_\beta[\mathbf{n}]$. So, we can use convolution to compute the response of the system to a discrete input. In the model, we first convolve the input data by the discrete impulse response $h_\alpha[\mathbf{n}]$ where $\alpha = \frac{\pi}{\lambda d}$ and then multiply by the lenslet array phase distribution $LA[\mathbf{n}]$ and we finally obtain the elemental images by convolving the result by $h_\beta[\mathbf{n}]$ where $\beta = \frac{\pi}{\lambda g}$. Note that we omitted the constants in the discrete versions of the kernel in order not to clutter the computations. The discretization issues related to diffraction are discussed in [10]. The parameters during the holographic recording must be known before we start. If

there is a mismatch between the recording parameters and the display parameters, we should process the hologram to match the parameters of these two steps. This is necessary because we want to focus the elemental images at the output.

During the process, we wish to first back propagate the holographic data to a location which we call the “origin”. The origin is defined as the effective depth of the nearest point of the object to the lenslet array.

In case of a mismatch between the physical parameters of the holographic recording step and our display the matching process is equivalent to equating the corresponding discrete Fresnel kernels. To find the relation between the kernels, let us assume that $h_{\alpha_1}[\mathbf{n}]$ represents the propagation associated with the holographic input setup parameters and the kernel $h_{\alpha_2}[\mathbf{n}]$ represents the propagation with the integral imaging setup parameters. If we equate the quadratic phases in $h_{\alpha_1}[\mathbf{n}]$ and $h_{\alpha_2}[\mathbf{n}]$, we can find the relation that matches the physical parameters. Let $\exp[j\alpha_1\mathbf{n}^T\mathbf{n}]$ be the quadratic phase in the Fresnel kernel representing the 2D diffraction field of the holographic setup where $\alpha_1 = \frac{\pi X_1^2}{(\lambda_1 z_1)}$, λ_1 is the wavelength, z_1 is the propagation distance, X_1 is the sampling period of the field in both directions. $\mathbf{n} = [n_1 \ n_2]^T$ where n_1, n_2 are integers. Let $\exp[j\alpha_2\mathbf{n}^T\mathbf{n}]$ be the quadratic phase in the Fresnel kernel representing the 2D diffraction field of the integral imaging setup where $\alpha_2 = \frac{\pi X_2^2}{(\lambda_2 z_2)}$. If we equate the parameters of these functions $\forall n$, we get, $\alpha_1 = \alpha_2$ thus $\frac{\pi}{(\lambda_1 z_1)} X_1^2 = \frac{\pi}{(\lambda_2 z_2)} X_2^2$. So, we can find that $z_2 = z_1 \cdot \frac{\lambda_1}{\lambda_2} \cdot \frac{X_2^2}{X_1^2}$. So, back-propagating the input data by z_2 is equivalent to placing the 3D object effectively at the origin as in Fig. 2(a).

2.2. The algorithm

The algorithm is given by the flowchart shown in Fig. 3. The input of the algorithm is diffraction data. Additional preprocessing steps may be needed depending on the nature of input data and the desired quality of the output display. For example, if the input is not from an object with a diffusing surface, we may need to multiply the associated field with a random phase to improve the visibility at the output. Also, for the cases where the recording physical parameters do not match with the display system parameters and where the object size is small compared to the display size, we may need to pre-process the data. The procedures for such cases will be discussed in detail later in this section. However, here we should mention that for all these cases, we first want to find the complex object field at the origin and then apply the specified processes. Actually, this step is not a necessity. On the contrary, we can generate the elemental images with the given diffraction pattern directly. To cover all cases by a single uniform step, we first back-propagate all input to the origin, and then apply the fixed process as described in Fig.2(c). This will then directly give the elemental images regardless of the properties of the original data.

We use the DFT method to compute the convolution to find outputs of the discrete systems. However, our discretized signals have a support that span both sides of the axes; i.e. n_1, n_2 can take zero, positive or negative values. Therefore, we must modify the commonly used DFT definition to operate also on such signals. Suppose that for a finite length signal $x[\mathbf{n}]$, $n_1, n_2 = -N/2, \dots, N/2 - 1$ we define the modified finite length $D\hat{F}T X[\mathbf{k}] = D\hat{F}T\{x[\mathbf{n}]\}$, $k_1, k_2 = -N/2, \dots, N/2 - 1$ as follows: Let the periodic $\tilde{X}[\mathbf{k}]$ be given by,

$$\tilde{X}[\mathbf{k}] = \sum_{n_1=0}^{N-1} \sum_{n_2=0}^{N-1} \tilde{x}[\mathbf{n}] e^{-j \frac{2\pi}{N} \mathbf{k}^T \mathbf{n}} \quad k_1, k_2 \in (-\infty, \infty) \cdot \quad (2)$$

Here, $\tilde{X}[\mathbf{k}]$ and $\tilde{x}[\mathbf{n}]$ are periodic extensions of finite length $X[\mathbf{k}]$ and $x[\mathbf{n}]$, respectively, as, $\tilde{X}[k_1 - N/2, k_2 - N/2] = X[(k_1)_{modN} - N/2, (k_2)_{modN} - N/2]$, and $\tilde{x}[n_1 - N/2, n_2 - N/2] =$

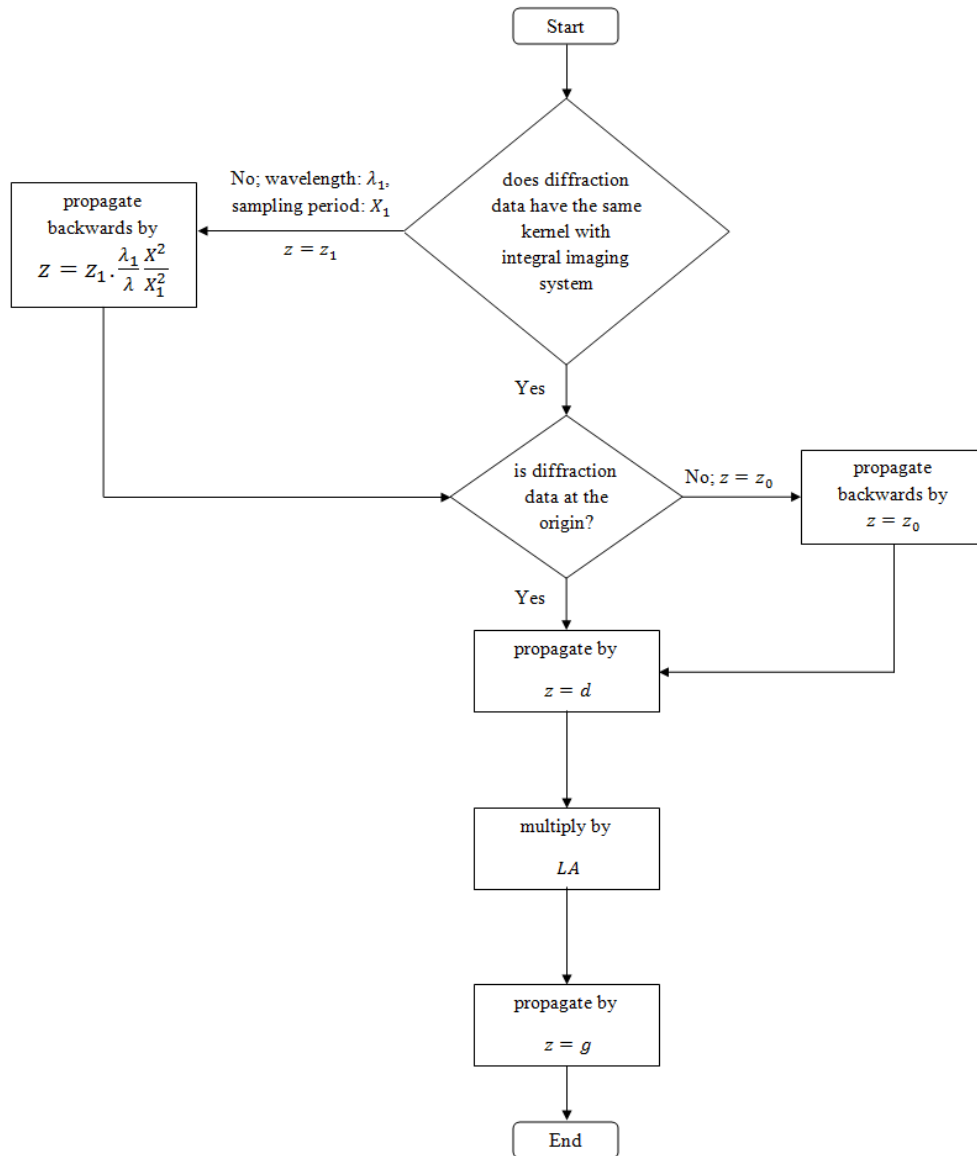


Fig. 3. The algorithm to generate elemental images from a diffraction pattern.

$x[(n_1)_{\text{mod}N} - N/2, (n_2)_{\text{mod}N} - N/2]$, n_1, n_2 are integers $(-\infty, \infty)$ and consequently, $X[\mathbf{k}]$ is one period over $k_1, k_2 = -N/2, \dots, N/2 - 1$ of $\tilde{X}[\mathbf{k}]$ and $x[\mathbf{n}]$ is one period over $n_1, n_2 = -N/2, \dots, N/2 - 1$ of $\tilde{x}[\mathbf{n}]$. In order to avoid aliasing that might be caused by the periodicity associated with DFT, while using this method, the computation window size should be selected sufficiently larger than the signal window in both directions. Outside the signal window, we chose to pad the computation window with zeros (opaque borders). Thus, we compute the linear convolution of the signals by approximating the circular convolution by padding zeros in the computation array. Moreover, this way, we simulate the case where those points on the object surface are the only possible source points. In our examples, the signal window sizes are chosen smaller than 1920×1920 while the computation window sizes are chosen as 3840×3840 . The Fresnel diffraction kernel is used to model wave propagation. Let us denote the signal window by $t[\mathbf{n}]$. The diffraction pattern, $t_d[\mathbf{n}]$, of the signal is calculated by

$$t_d[\mathbf{n}] = ID\hat{F}T \{ D\hat{F}T \{ w_t[\mathbf{n}] \} H_\theta[\mathbf{k}] \} \quad (3)$$

where $\mathbf{n} = [n_1 \ n_2]^T$ and $\mathbf{k} = [k_1 \ k_2]^T$ represent the discrete spatial domain variables and the discrete spatial frequency domain variables, respectively, and n_1, n_2, k_1, k_2 are integers; we choose the range for n_1, n_2, k_1 and k_2 as $[-1920, 1919]$ in our examples. $w_t[\mathbf{n}]$ is the computational window and $t[\mathbf{n}]$ is centered inside $w_t[\mathbf{n}]$. 2D $D\hat{F}T$ and 2D $ID\hat{F}T$ of the matrices are computed using 2D FFT and 2D IFFT algorithms, respectively.

In order to speed up the computations, we used the Fresnel kernel in the spatial frequency domain. The Fourier transform of continuous Fresnel kernel is

$$H(\mathbf{f}) = \exp\left(j\frac{2\pi}{\lambda}z\right) \exp(-j\pi\lambda z \mathbf{f}^T \mathbf{f}) \quad (4)$$

where $\mathbf{f} = [f_x \ f_y]^T$, f_x and f_y are the spatial frequency domain variables in cycles per unit distance in $(-\infty, \infty)$. To compute the discrete Fresnel kernel, we discretize Eq. (4) by substituting \mathbf{f} with $\mathbf{U}\mathbf{k}$ and we obtain

$$H_\theta[\mathbf{k}] = \exp(-j\theta \mathbf{k}^T \mathbf{U}^T \mathbf{U} \mathbf{k}) \quad (5)$$

where $\mathbf{k} = [k_1 \ k_2]^T$ and $k_1, k_2 = -N/2, \dots, N/2 - 1$, $U = \begin{bmatrix} 1/(NX) & 0 \\ 0 & 1/(NX) \end{bmatrix}$ is the 2D rectangular sampling matrix in the spatial frequency domain and $\theta = \pi\lambda d$. N is the total number of pixels along one side of the discrete 2D calculation array, X is the spatial sampling period and d is the propagation distance. We omitted the phase constant, which appears in Eq. (4), in order not to clutter the computations.

On the lenslet array plane, we generate the lenslet array complex phase pattern given as in [11]. A single lenslet of the array is given by

$$l[\mathbf{n}] = \exp(-j\gamma \mathbf{n}^T \mathbf{V}^T \mathbf{V} \mathbf{n}) \quad (6)$$

which is obtained by discretizing

$$l(\mathbf{x}) = \exp\left(-j\frac{\pi}{\lambda f} \mathbf{x}^T \mathbf{x}\right) \quad (7)$$

and by substituting \mathbf{x} by $\mathbf{V}\mathbf{n}$ where n_1, n_2 are in the interval $[-M/2, M/2 - 1]$ and $\gamma = \frac{\pi}{\lambda f}$, $V = \begin{bmatrix} X & 0 \\ 0 & X \end{bmatrix}$ is the 2D rectangular sampling matrix in the spatial domain. We chose the focal length as $f = M\frac{X^2}{\lambda}$ to cover the entire normalized frequency range in the interval $[-\pi, \pi]$ radians where M is the length of one side of a lenslet. A 2D array of lenslets, $LA[\mathbf{n}]$, is generated

by replicating $l[\mathbf{n}]$ in both directions in a rectangular fashion. $LA[\mathbf{n}]$ is centered within the computation window $w_{LA}[\mathbf{n}]$. Also, the lenslet array is large enough to image most of the light scattered from the object. $w_{LA}[\mathbf{n}]$ is multiplied with the diffraction pattern, $t_d[\mathbf{n}]$, of the object. Focal length of the lenslets is chosen such that it satisfies the imaging equation $1/f = 1/g + 1/d$ and proper magnification ratios are obtained at the imaging plane. To give numerical examples, we chose $f = 10.8mm$ and $d = 7f$. Finally, we calculate the diffraction pattern due to the resulting complex field of the multiplication $w_{LA}[\mathbf{n}]t_d[\mathbf{n}]$ at the imaging depth, g . The resultant complex diffraction pattern is given by

$$p[\mathbf{n}] = ID\hat{F}T \{ D\hat{F}T \{ w_{LA}[\mathbf{n}] t_d[\mathbf{n}] \} H_\sigma[\mathbf{k}] \} \quad (8)$$

where $\sigma = \pi\lambda g$. Taking the square magnitude of this pattern simulates the discrete intensity recording,

$$I[\mathbf{n}] = |p[\mathbf{n}]|^2. \quad (9)$$

As a result, we obtain computer generated elemental images of the 3D object.

2.3. The examples

Now we will proceed with the examples of three different input diffraction patterns, as a proof of the concept, we chose three examples. In the reconstructions, we demonstrate the depth of focus, viewing angle and parallax of our display, qualitatively. The first example is a set of two planar letters; the letters are at different depths. Such an example is extensively used in the literature [4, 5, 7]. This example helps us to understand whether we are able to distinguish different depths in the reconstructions. Also, it gives an idea about the depth of focus of the lenslets. Our second example is an extension of the first one. We sliced down a pyramid object to create several planar objects. This time our aim is to show the parallax that can be obtained using our display. Since, we have a depth variation in the object, it is easier to observe the parallax effect. The last example presents the most important aspect of our method. We used a digitally obtained optical diffraction tomography data as the input of our method. We can generate elemental images even from such physical data.

In the first example, we have two different digital letters at two different depths. One letter is located at the origin, and the other one is located at $z = -5f$ where $f = 10.8mm$. These letters are separated along the x -axis by $2.6mm$. The amplitude of the object points on the letters are taken as 1 and the other points outside the letters are 0. Let the letter located at distance $z = -5f$ is represented by the computation window $w_{t_1}[\mathbf{n}]$ and the other is represented by $w_{t_2}[\mathbf{n}]$. So, we have two slices in the space. To find $w_t[\mathbf{n}]$ we perform the following computation:

$$w_t[\mathbf{n}] = ID\hat{F}T \{ D\hat{F}T \{ w_{t_1}[\mathbf{n}] R_1[\mathbf{n}] \} H_\eta[\mathbf{k}] \} + \{ w_{t_2}[\mathbf{n}] R_2[\mathbf{n}] \} \quad (10)$$

where $\eta = \pi\lambda(5f)$, $R_i[\mathbf{n}]$, $i \in \{1, 2\}$, is a random matrix with entries $R_i[\mathbf{n}] = [r_{n_1 n_2}]$ where $r_{n_1 n_2} = \exp(-j2\pi\mathcal{X})$ and where \mathcal{X} is a random variable uniformly distributed in $[0, 1]$. Thus, the window $w_{t_1}[\mathbf{n}]$ is first multiplied by a random phase $R_1[\mathbf{n}]$ and then propagated by an effective distance of $5f$. The result is added to $w_{t_2}[\mathbf{n}]$ which is also multiplied by another random phase factor. The second slice is not propagated since it is already located at the origin. The assumption is that, the multiple diffraction effects from each slice of the object are negligible. Thus, each slice is assumed to contribute to the diffraction field independently of others. This is because, the multiplication with the random phase simulates diffusing surfaces, and thus, ensures that the light traveling in the space well scatters almost everywhere. To note that, the object at $z = -5f$ distance will be $5f$ in front the object at the origin in the reconstruction. So, the object at the origin will be reconstructed at $d = 7f$, which is the distance we chose while generating the elemental images, and the other object will be observed at $12f$. The generated



Fig. 4. Computed and recorded elemental images of two letters at different depths and positions. (We enhanced the brightness of the figure for visual purposes. This is achieved by stretching the contrast. The figure is also used on the LCD display of the integral imaging setup as is. Similar enhancement procedure is used in Figs. 6, 8 and 14-17. In Figs. 14-17, we enhanced only the computer simulation results.)

elemental images set is given in Fig. 4. The second example is a pyramid object. This time we have several slices of a pyramid object; a sketch is shown in Fig. 5. Only six slices are shown in Fig. 5 for clarity. However, we chose to simulate with nine slices. Only the base part of the pyramid is a full frame. And only the tip of the pyramid is a single square patch. At each other slice, we have square patches located at the corners on the edges. When looking from the center, each slice containing square patches can be seen clearly, that is, any patch do not obscure the others including the base frame and the tip. This is a coarse quantization of a wire-frame pyramid structure. To make a reconstruction where the tip is at the front and the base frame is at the back, the base frame ($w_{i_0}[\mathbf{n}]$) is located at the origin and tip ($w_{i_8}[\mathbf{n}]$) is located at $z = 24mm$. We chose such a size because, we had a similar size physical wire-frame pyramid, which is also used in [28], to compare the optical reconstructions. The base frame of this physical pyramid is a square with an edge size of $8mm$. In the simulations, the pixel size of this edge is 960 pixels. The width of the patches and the wire-frame is 60 pixels. $w_t[\mathbf{n}]$ is computed as,

$$w_t[\mathbf{n}] = \sum_{i=0}^8 ID\hat{F}T \{ D\hat{F}T \{ w_{i_t}[\mathbf{n}] R_i[\mathbf{n}] \} H_\eta[\mathbf{k}] \} \quad (11)$$

where $\eta = \pi\lambda(i\Delta)$ and $\Delta = 24mm/8 = 3mm$. Note that $H_\eta[\mathbf{k}] = 1$ when $\eta = 0$. Fig.6 shows the elemental images of the pyramid object. The last example is physically captured diffraction data obtained by a diffraction tomography technique [22]. The object is an epithelium cell, which is mostly a transparent (phase) object. Since it has a small depth, it is harder to see the 3D volume and perceive the parallax. Moreover, a coherent illumination is used while obtaining the diffraction pattern. Furthermore, the size of the data is small pixel-wise, so, we zoomed the input data to perceive a larger object. All of these issues are handled as follows: To zoom the object, we interpolated the 2D signal. To do that, we upsampled the original diffraction data, $t_{captured}[\mathbf{n}]$, by a factor of two in both directions ($K = 2$) and then low pass filtered (half

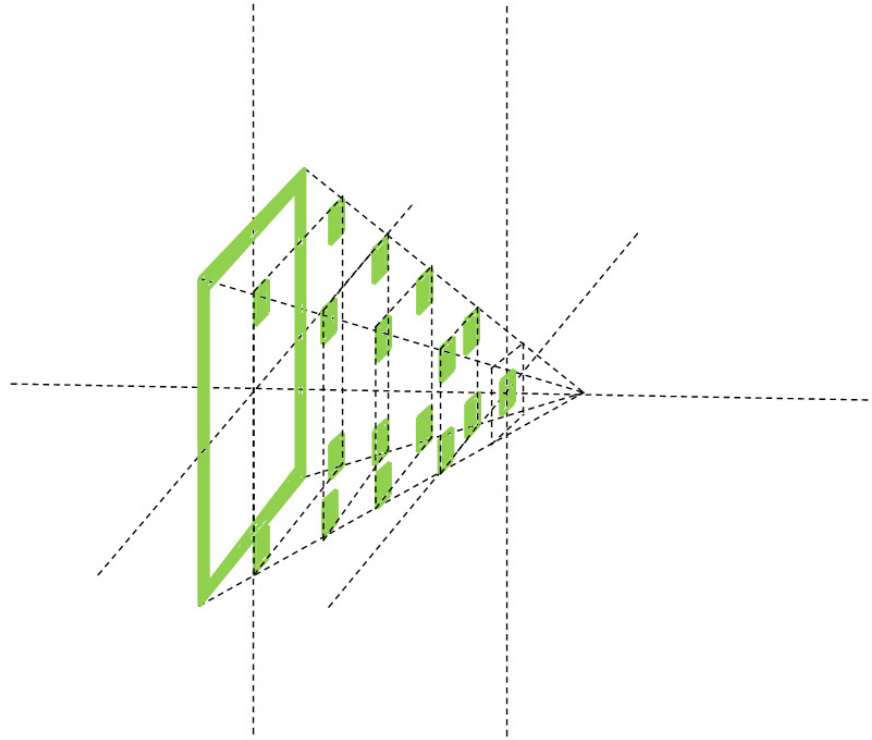


Fig. 5. A sketch of the pyramid object. A square pyramid is sampled (sliced) over the z -axis. Base part is a square frame while the edges and the tip of the pyramid are small square patches. For display purposes we showed six slices of the object whereas in the simulations we used nine slices.

band filter) the result and obtained $t_{interpolated}[\mathbf{n}]$. This method does not degrade the diffraction pattern. The result can be seen in Fig. 7. The diffraction data was captured at a certain distance, $z = z_1$. First, we will propagate this data backwards to the origin as it is shown in the flowchart in Fig. 3. However, since we upsampled the data, the required propagation distance become $z = K^2 z_1 \frac{\lambda_1}{\lambda} \frac{X^2}{X_1^2}$. Thus the pre-processed signal (complex field) becomes,

$$t_{object}[\mathbf{n}] = IDFT \{ DFT \{ t_{interpolated}[\mathbf{n}] \} H_{\eta}[\mathbf{k}] \} , \quad (12)$$

where $\eta = \pi \lambda \left(K^2 z_1 \frac{\lambda_1}{\lambda} \frac{X^2}{X_1^2} \right)$ which is simply $\eta = \pi \lambda_1 \left(K^2 z_1 \frac{X^2}{X_1^2} \right)$. We now, insert this signal into the center of the computation window $w_t[\mathbf{n}]$, thus, we have the diffraction field at the origin. At this point, the complex diffraction data contains the three-dimensional information of the object. Depending on the depth of the object, only certain parts of the object are seen in focus if the magnitude of this field is imaged. Since the object depth is shallow compared to the reconstruction distance, most of the object is in focus at the origin. We also do not know the diffusiveness of the complex object field. So, we choose to multiply the complex diffraction data with a random phase. Here, one should be careful while doing this operation since it might destroy the three-dimensional information. This can be visualized as putting a diffusive glass in

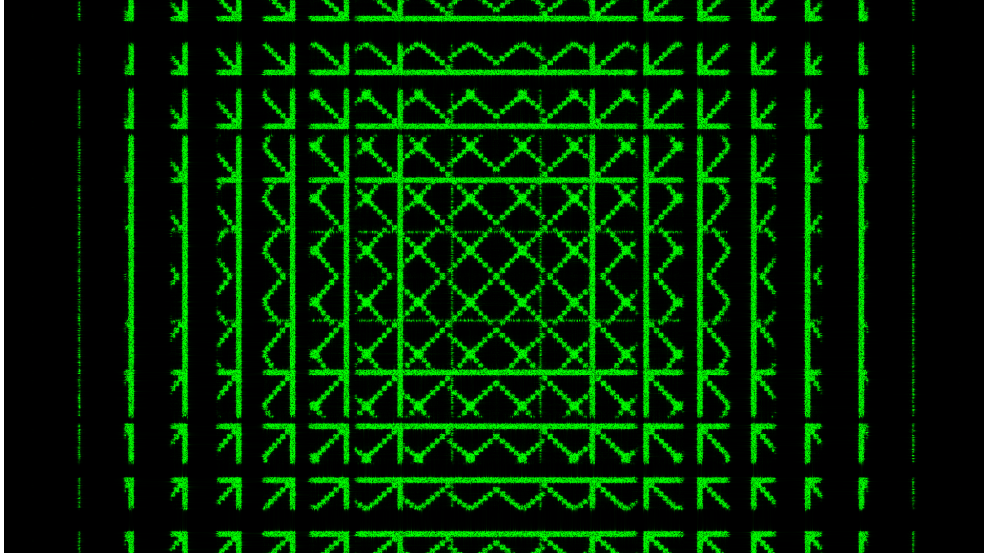


Fig. 6. Computed and recorded elemental images of the pyramid object. (We enhanced the brightness of the figure for visual purposes.)

front of an object. The parts closer to the glass can be seen well while the far away points will be obscure. Fortunately, this operation improves the performance of our method because the light will be reached and imaged by most of the lenslets. Furthermore, the visibility of the elemental images will improve. However, for those objects that have a rather large depth, this method may not work. Even if this step is skipped, the method would still work. However, this time, only those lenslets closer to the center of the lenslet array will image the 3D object. The ones at the periphery will not generate any image since the light from the object will not reach them. This will decrease the viewing angle of the reconstructed 3D image. So, multiplication by a random phase helps us to use the maximum viewing angle. We multiply $w_l[\mathbf{n}]$ with a random phase $R[\mathbf{n}]$. For this last example the elemental images are shown in Fig. 8. Note that, the elemental images obtained for the epithelium cell is filtered by a simple high pass filter to sharpen the edges and enhance the details of the object. We filtered the signal by a half band high pass filter. This improved the reconstruction quality, which is determined by subjective assessments. All of the examples need slightly different preprocessing. However, once we obtained $w_l[\mathbf{n}]$, the rest of the algorithm is the same for all cases. We also performed reconstruction simulations and compared them with the optical reconstructions. To simulate the reconstructions, we computed our algorithm in the reverse order. However, this time the input of the algorithm is the intensity distribution of the elemental images, $I[\mathbf{n}]$, at a single plane. We first multiplied the elemental images with a random phase $R[\mathbf{n}]$ and then propagate the result to a distance $z = g$, where the lenslet array is located. The complex field just before the lenslet arrays is given by

$$t_d[\mathbf{n}] = ID\hat{F}T \{ D\hat{F}T \{ I[\mathbf{n}] R[\mathbf{n}] \} H_\sigma[\mathbf{k}] \} . \quad (13)$$

We multiply this field with the lenslet array pattern, $w_{LA}[\mathbf{n}]$, as in the previous case. Finally, we propagate the field just after the lenslet array to a distance $z = d + \Delta d$, where d is the closest distance from the points on the object to the lenslet array and Δd is the additional distance to focus on the far away object points. We can focus at a certain plane by selecting this distance.

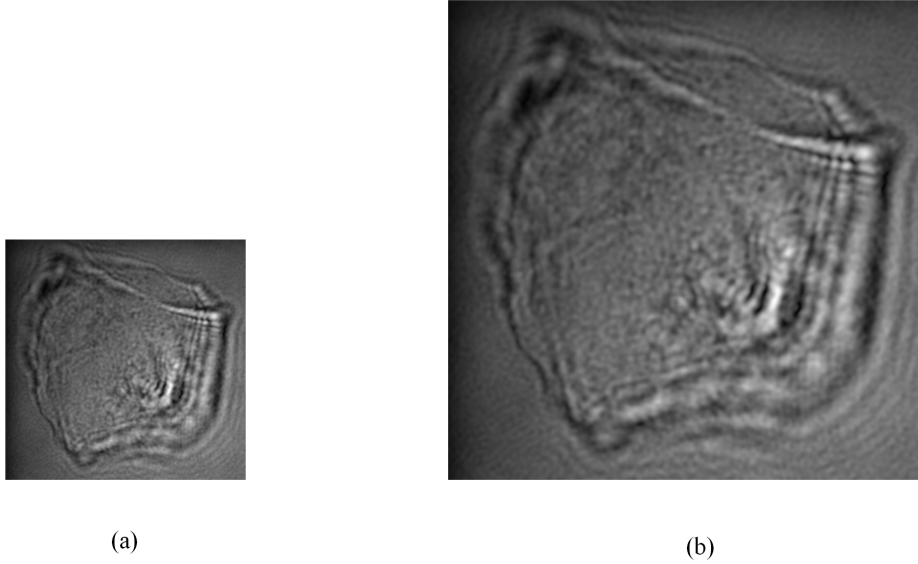


Fig. 7. (a) The amplitude picture of the diffraction pattern of the epithelium cell. (b) The upsampled (interpolated and low pass filtered) version of (a).

The intensity distribution on the focused plane is given by

$$r[\mathbf{n}] = \left| ID\hat{F}T \left\{ D\hat{F}T \left\{ w_{LA}[\mathbf{n}] t_d[\mathbf{n}] \right\} H_{\chi}[\mathbf{k}] \right\} \right|^2 \quad (14)$$

where $\chi = \pi\lambda(d + \Delta d)$. The simulation results for the reconstructions are given in Section 3.

2.4. Optical setup

The optical setup is depicted in Fig. 9. We display the elemental images on a Samsung T240 monitor. The resolution of the monitor is 1920×1200 pixels. Our elemental image set size is 1920×1080 pixels. So, we fit the image by leaving 60 pixels from top and bottom blank. The pixel size of the monitor is $0.27mm$ and the dimensions of the active area that we used was $518mm \times 292mm$. The lenslet array is written on a Holoeye HEO 1080P phase-only LCoS SLM, which is a high definition 1920×1080 pixels reflective type SLM. We write 20×12 lenslets on the SLM. Each lenslet has a size of 90×90 pixels with a focal length $f = 10.8mm$. Pixel size of the SLM is $8\mu m$, thus each lenslet size is $0.72mm \times 0.72mm$. With that many lenslets we can only fit a lenslet array with full size lenslets to an active area of 1800×1080 pixels on the SLM. The unused parts (60 pixel each) are left blank equally on the left and right side of the SLM. Thus, the active area size for the lenslet array was $14.4mm \times 8.64mm$. The lenslet array is shown in Fig. 10. Our setup is a typical integral imaging display setup. However, due to the size difference between the lenslet array and the LCD screen, we need to scale the elemental images on the LCD screen by the help of a projector objective. For this reason, we used a projector objective which is disassembled from a Epson EMP-TW520 projector. Since the SLM is reflective type, we put a non-polarizing beam splitter (NPBS) to illuminate and observe the reconstructed image. However, the NPBS changes the focal point of the lenslets [11]. Thus, for fine tuning, we tried to find a focused reconstruction while changing the position of the projector objective. The reconstructions are observed at the expected distances. The entire system, its

close-up view and the view from the viewing zone perspective are shown in Fig. 11, Fig. 12 and Fig. 13, respectively.

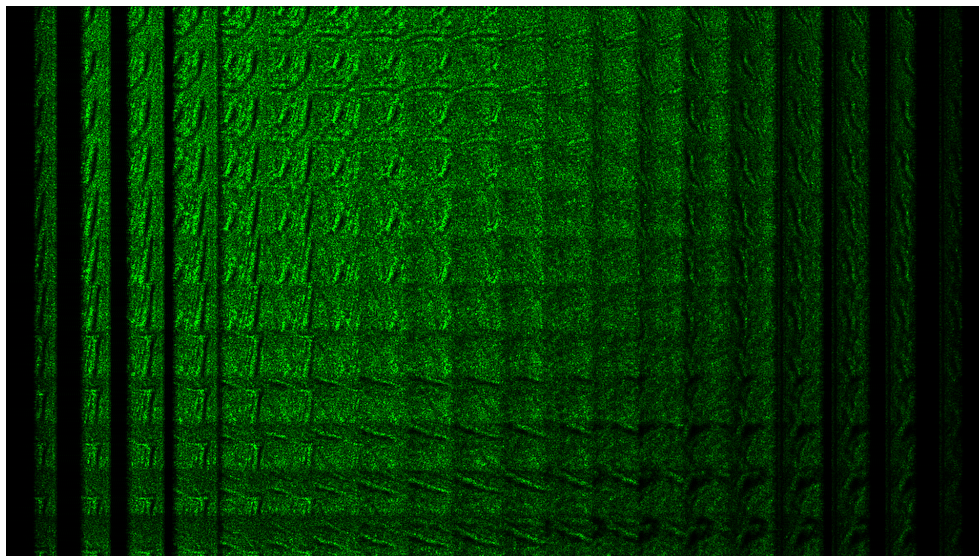


Fig. 8. Computed and recorded elemental images of the epithelium cell. (We enhanced the brightness of the figure for visual purposes.)

3. Results

We compared the computer simulation results and the optical reconstructions. Here we present the results for each example given in Section 2.3.

Our first example was two letters at different depths and location. To determine the focused planes we put two cards with “Bilkent University” label on them as shown in Fig. 13. The card, where the label is horizontally aligned, is located $8.4f$ distance away from the SLM surface. The one with the label, which is vertically aligned, is located approximately at $13f$ away from the SLM surface. When we display the elemental images in Fig. 4, we observed the reconstructions as in Fig. 14. In this figure, the top images are computer simulation results while the bottom images are the optical reconstructions. The images on the left shows the reconstructed object at $8.4f$ while the right images are the reconstructions of the object at $13f$. The letter “A” is seen sharper than the letter “Z”. This is due to the depth of focus of the lenslets. We exaggerate the distances to show that the system works. For a closer capture distance, for the letter “Z”, the reconstructions would be sharper. As we explained in Sec. 2.4, the NPBS shifts the focal distance of the lenslets. We also confirmed these shifted location by computer simulations.

For the second object, the pyramid, we performed two experiments. The first experiment is to show the depth of the object and the second one is to show the parallax. In Fig. 12, we show how we modified the setup. In Fig. 15, left images are the computer simulation results and the right images are the optical reconstructions together with a physical wireframe pyramid object with the same size as the reconstruction. The top two images show the focusing to the tip of the pyramid. The depth of the object is $24mm$ as mentioned in Section 2.2. The base part of the pyramid, which is located $8.4f$ away from the SLM surface, is shown in focus in the bottom part of Fig. 15. For the parallax experiment, we shoot photos from three different viewing

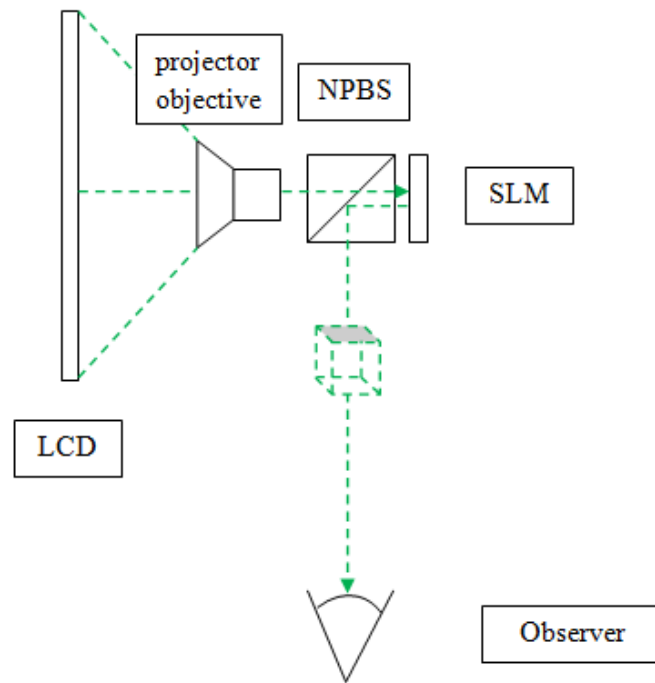


Fig. 9. The optical setup

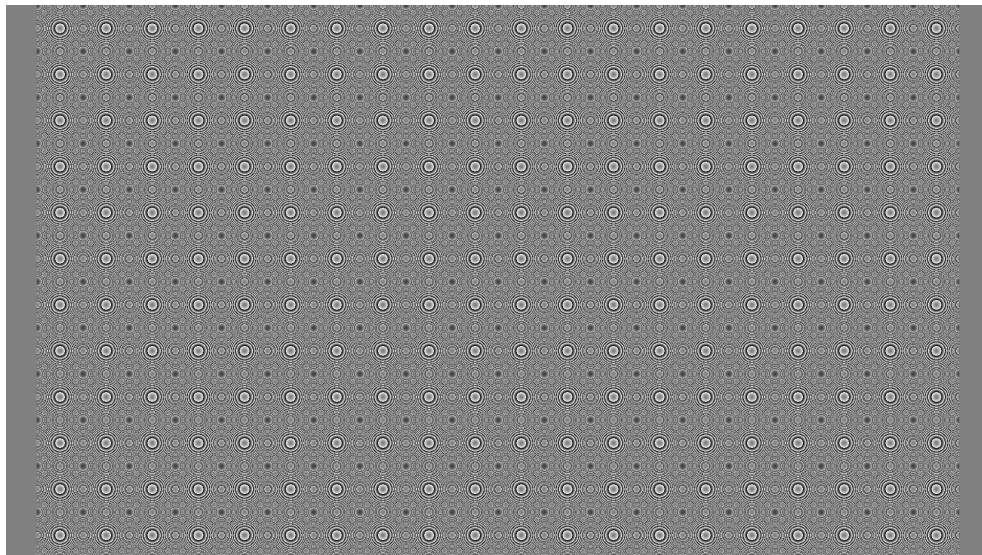


Fig. 10. A Fresnel lenslet array pattern with 12×20 lenslets. Each lenslet has a focal length of 10.8mm . We excluded the lenslet on either side of the array since they would be cropped if we have included them. Instead we left 60 pixels blank from either side of the array that is written on the 1920×1080 pixels phase only LCoS SLM.

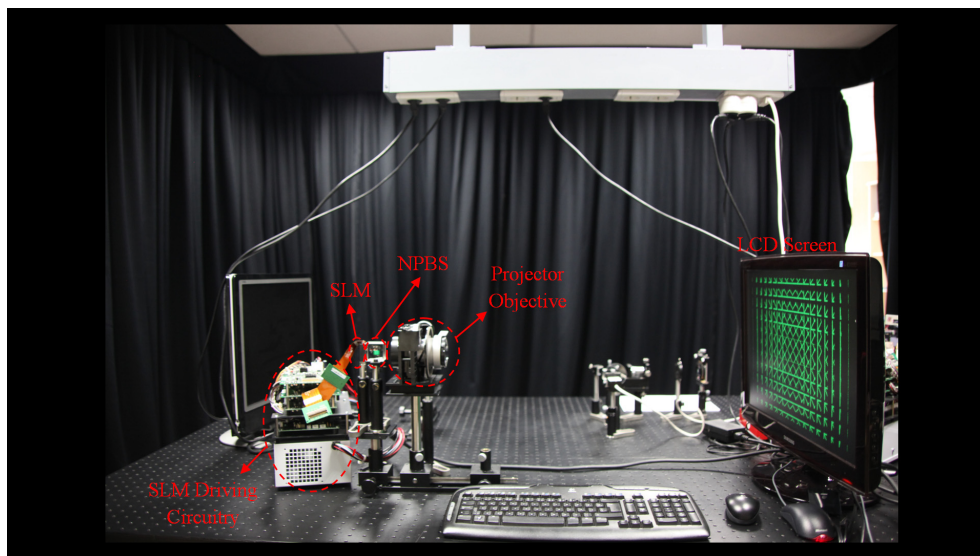


Fig. 11. Picture of the entire optical setup.

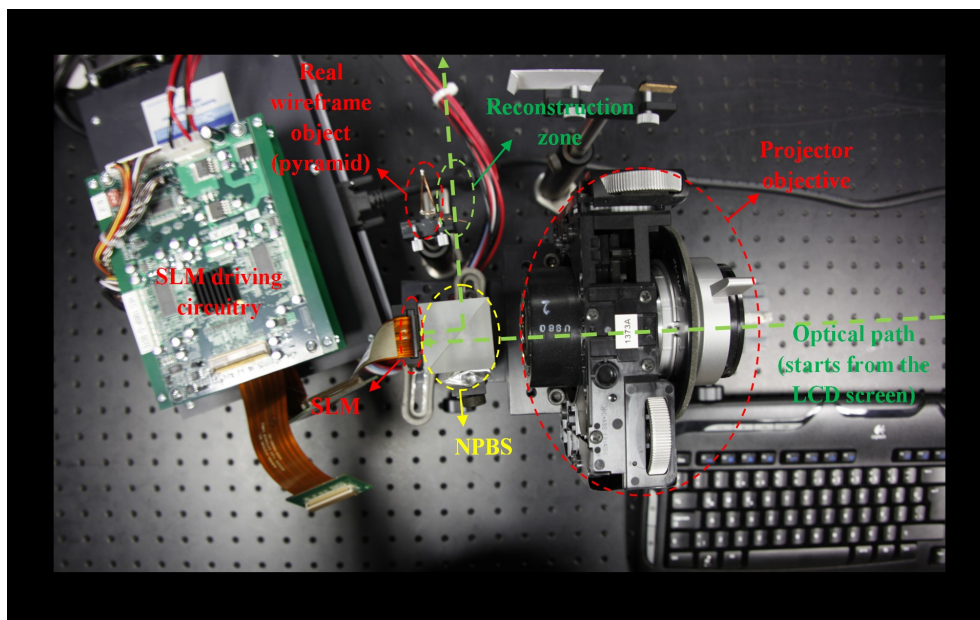


Fig. 12. Top view of the optical setup. There is a wireframe pyramid object next to the reconstruction zone. It is used to compare the reconstructed 3D images of the pyramid object.

angles from left to right. We focused to the tip in order to show the parallax better. In Fig. 16, the top three images are computer simulations for the parallax, while the bottom pictures are the optical reconstructions. This effect can be seen better with the optical reconstructions. However, the viewing angle of the system, is limited with the maximum diffraction angle of the SLM device, $\omega = \frac{\lambda}{X} = \frac{532nm}{8\mu m} = 0.067rad \approx 4^\circ$, [6, 14]. The aliased components appear when we go to higher angles to observe the reconstruction. This is seen both in the optical reconstruction and in the computer simulations. Viewing angle of this system can be improved by decreasing the pixel period, X , of the SLM device or by introducing multiple SLM circular configurations [29–31].

The last example was the epithelium cell object. The top image in Fig. 17 shows the computer simulation results. The bottom image shows the reconstruction at $8.4f$. Since the object has a small depth, it is not possible to observe a 3D effect or the parallax. However, we showed with this last example that it is possible to convert holographic recording, regardless of the acquisition method (numerical data generation or digital recording of optical data), to elemental images and reconstruct them successfully by numerical or optical means.

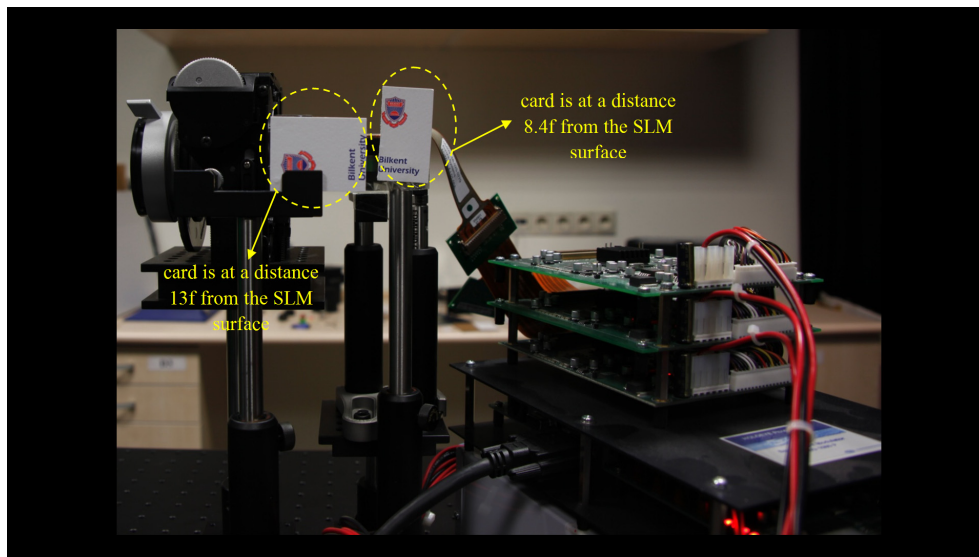


Fig. 13. The viewing zone of the optical setup. We placed cards labeled as “Bilkent University” at different distances in order to check the reconstruction distances.

4. Conclusion

We demonstrated a method to convert digitally computed (synthetic) or digitally recorded holographic (physical) data to elemental images. Synthetic (computationally generated) or digitally recorded physical data are processed to obtain elemental images of the original 3D objects. Our proposed method is based on diffraction calculations, instead of commonly used ray tracing methods, to generate elemental images from digitally available 3D data. We showed three examples: two letters at different depths, a pyramid object and a hologram of a real epithelium cell that is obtained by diffraction tomography. Both digitally simulated reconstructions (obtained using diffraction calculations) and optical reconstructions are compared for these three examples. Optical reconstructions are obtained from an integral imaging display setup. The lenslet array of the integral imaging display consists of a phase-only SLM with a Fresnel

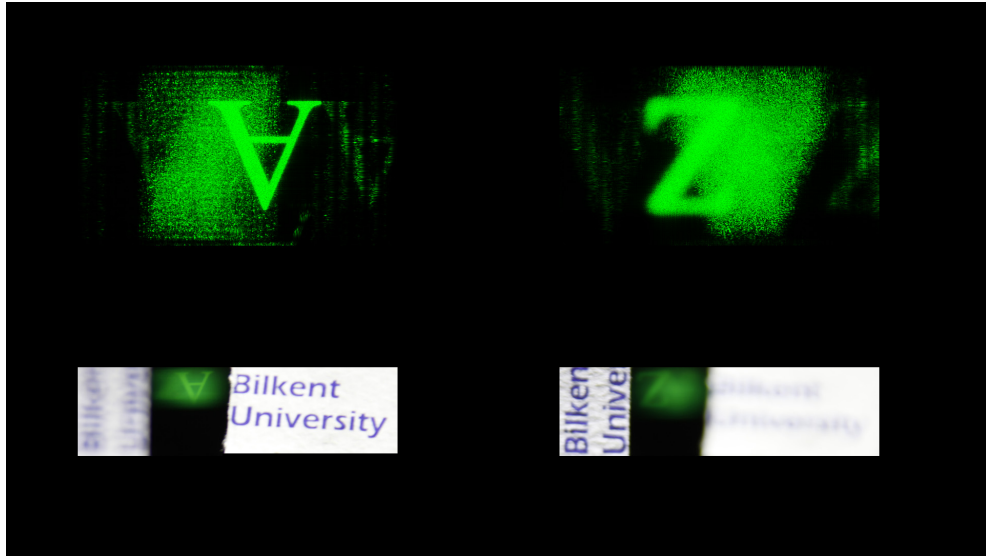


Fig. 14. 3D reconstruction from the elemental images of Fig. 4. At the top, digital reconstructions are shown while at the bottom we observe the optical counterparts. On the left side, the camera, which took this picture, was focused to a distance $8.4f$ and on the right side, it was at $13f$. (We enhanced the brightness of the computer simulation results for visual purposes.)

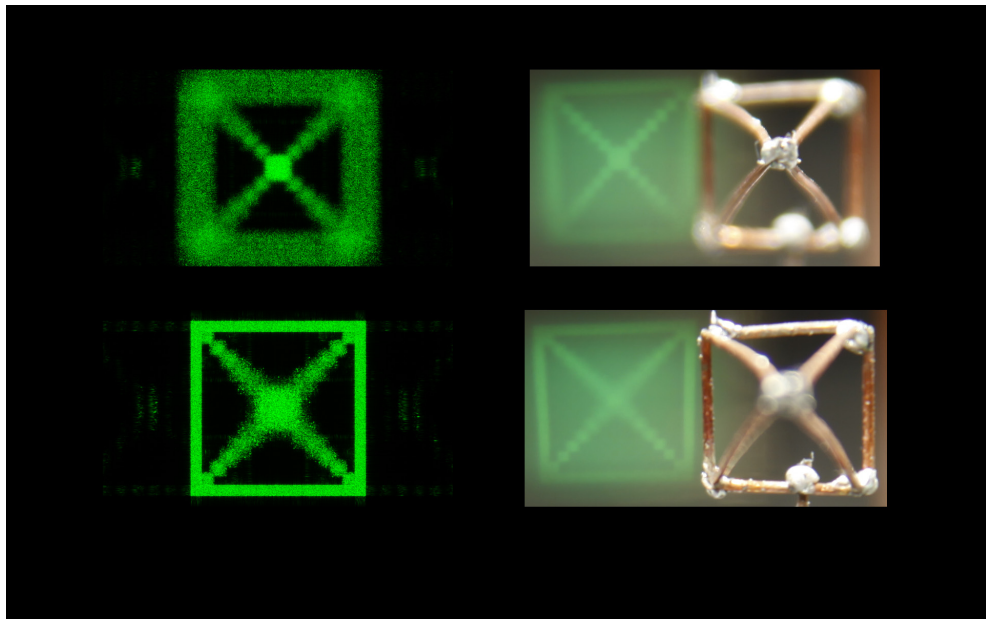


Fig. 15. 3D reconstruction from the elemental images of Fig. 6. Images at the left are digital reconstructions. Images at the right are optical reconstructions. The top images are focused to the tip of the pyramid object and the images at the bottom are focused to the base of the object. It is clearly seen that the physical (wire) object and the reconstructed 3D images match. (We enhanced the brightness of the computer simulation results for visual purposes.)

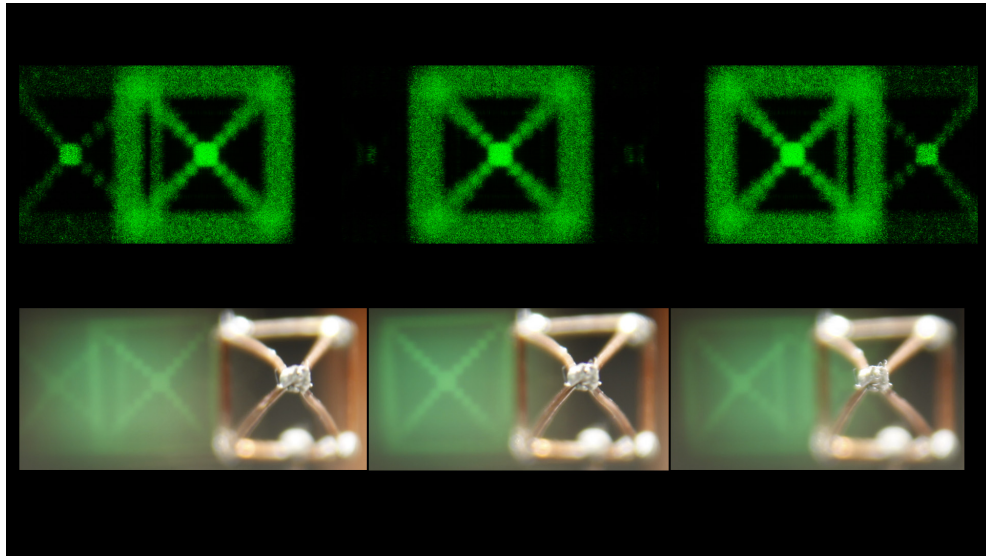


Fig. 16. The pictures of the pyramid image taken from three different angles. (All are focused to the tip of the pyramid.) The pictures at the top are the digital reconstructions and the bottom ones are the optical reconstructions. The pictures show the parallax and the viewing angle. (We enhanced the brightness of the computer simulation results for visual purposes.)

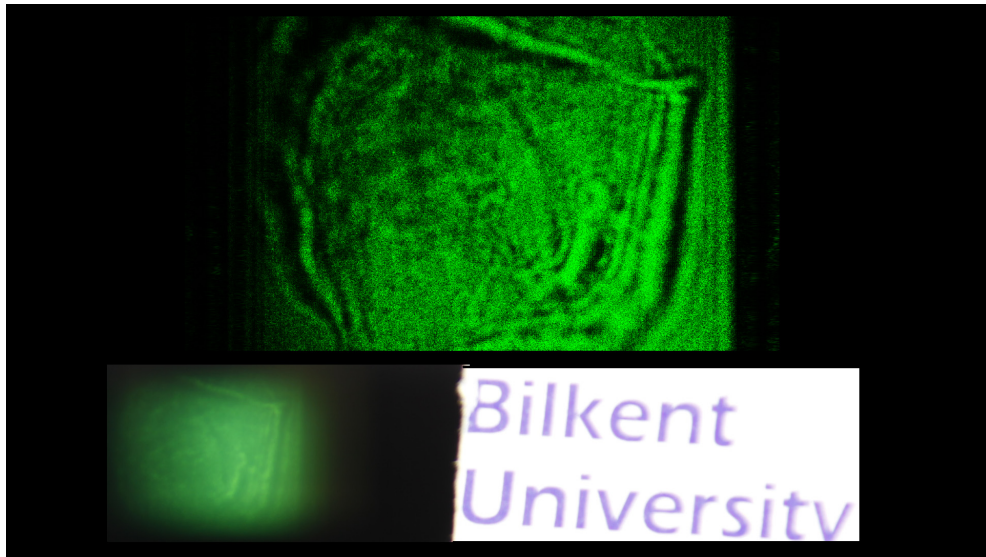


Fig. 17. Reconstruction from the elemental images of Fig. 8. Top picture is the digital reconstruction whereas the bottom one shows the optical reconstruction. Since the object thickness is small relative to the reconstruction distance, a 3D depth is not perceived. However, the planar looking thin object still floats in 3D space. (We enhanced the brightness of the computer simulation results for visual purposes.)

lenslet array pattern written on it. The optical reconstructions provide satisfactory results. The first example gives an idea about the depth of focus of the digital lenslet array. We showed with the synthetic 3D pyramid object example that the display provides a good parallax, which is limited by the maximum diffraction angle of the SLM. We also compared the reconstruction with a physical wire-frame pyramid object and it confirmed that our system works well within its physical limitations. We also showed that we can use digitally captured optical diffraction data to computationally generate a set of elemental images and reconstruct the 3D image of the cell from these elemental images on a physical integral imaging display. Our proposed display system and the method for obtaining elemental images make it possible to display holographic recordings on an integral imaging display setup.

Acknowledgments

This work is supported by the European Commission within FP7 under grant 216105 with the acronym Real 3D. We thank Isabelle Bergoënd and Christian Depeursinge from EPFL for the epithelium cell diffraction data they provided. A. Özgür YÖNTEM thanks TÜBİTAK for the scholarship he received during his doctoral studies.